Beam halo from Touschek scattering in the KEK Accelerator Test Facility*

Renjun Yang,[1,2] Alexander S. Aryshev,[3,4] Philip Bambade,[5] Michele Bergamaschi,[6]
Kiyoshi Kubo,[3,4] Takashi Naito,[3,4] Nobuhiro Terunuma,[3,4] and Sandry Wallon[5]

[1] *Institute of High Energy Physics, Chinese Academy of Sciences, Beijing 100049, China*
[2] *Spallation Neutron Source Science Center, Dongguan, 523803, China*†
[3] *High Energy Accelerator Research Organization, Tsukuba 305-0801, Japan*
[4] *School of High Energy Accelerator Science, SOKENDAI, Tsukuba 305-0801, Japan*
[5] *IJCLab, CNRS/IN2P3, Université Paris-Saclay, Orsay 91898, France*
[6] *European Organization for Nuclear Research, Geneva CH-1211, Switzerland*

Beam halo is one of the most crucial issues limiting the machine performance and causing radioactivation in high-intensity accelerators. From the diagnostics point of view, the beam halo is of low density and challenging to observe. For high-luminosity colliders, modern light sources and spallation neutron sources, a clear picture of beam-halo formation is of great importance for successfully suppressing the undesired beam loss by employing a dedicated collimation system. The Accelerator Test Facility (ATF) of KEK has been constructed to study the feasibility of producing the low-emittance beam required at a linear lepton collider and nanobeam focusing & control techniques. On the other hand, it supplies an excellent opportunity for the experimental investigation of beam-halo formation in a GeV storage ring. This article presents numerical and experimental studies of transverse and longitudinal halos in the KEK Accelerator Test Facility. The general consistency between predictions and observations in various conditions indicates that the Touschek scattering is the dominant mechanism forming the horizontal and momentum halos.

Keywords: beam halo, Touschek scattering, Accelerator Test Facility

I. INTRODUCTION

Beam halo is one of the most critical issues limiting the performance and potentially causing component activation of high-intensity accelerators, especially high-energy colliders at the luminosity frontier. However, a general definition of "halo" is complicated because it should be given in align with the requirements of machine operation and the primary concerns of beam loss. From the diagnostic point of view, one thing is undoubtedly clear–by definition, beam halo is of low density and difficult to measure. In some literature, the complete beam profile is divided into three parts referring to the beam centre: core, tail and halo [1]. However, the boundary between the tail and the halo is rather ambiguous. As a consequence, hereinafter, beam halo presents both tail and halo particles without additional specifications. The formation of beam halo is generally complex and associated with collective effects, nonlinearities, optics errors, beam-beam interaction, secondary emission, and so on [2–11]. The collimation system has been a fundamental part of a high-intensity accelerator to mitigate the undesired background induced by halo-particle loss. To estimate the collimation efficiencies and the residual backgrounds at a required level of accuracy, knowledge of the primary driving mechanisms and beam halo modelling is vital. Moreover, a clear picture of halo formation can help to predict the detector background around sensitive regions, e.g., the injection area and the interaction point. To accomplish this task, both simulations with various physical processes and observations employing a powerful halo monitor with sufficient dynamic range are required. The dynamic range in the context of this article is the inverse ratio of the smallest resolvable fractions of a large quantity, in our case the number of particles, to the maximum of that quantity. Massive tracking simulations in the presence of realistic machine imperfections and primary collective effects are typically necessary to provide a reasonable prediction of beam halo. Regarding the halo diagnostics, even though one can sample the halo regions using a sensitive monitor with a standard dynamic range, a complete profile imagined with a high-dynamic-range monitor is more desirable. In principle, many profile monitors could be adapted for direct observation of beam halo after necessary upgrades. For an electron accelerator, a halo diagnostic based on the optical method is typically favoured to obtain a satisfactory dynamic range.

The Accelerator Test Facility (ATF) at KEK was initially constructed to demonstrate the feasibility of producing low-emittance beams required at a future linear collider and supply high-quality beams for the R&D activities on beam dynamics, instrumentation and control technology, which will be needed at future accelerator-based facilities [12–15]. ATF provides an excellent opportunity to investigate halo formation towards future high-energy accelerators. Compared with a high-energy collider with a high local chromaticity in the interaction region and strong nonlinear beam-beam interaction effects, the primary mechanisms driving particles into the halo region in a GeV-scale electron storage ring are more straightforward, involving mainly beam-gas scattering (BGS), Touschek scattering and nonlinearities [16–18]. However, the verification of such plausible driving mechanisms from direct observations has been rarely reported. Precedent beam halo studies in ATF have concentrated on the

* Supported by the National Natural Science Foundation of China (No.12305166), Toshiko Yuasa France-Japan Particle Physics Laboratory (project A-RD-10), the MSCA-RISE E-JADE project, funded by the European Commission under grant number 645479.

† Corresponding author, yangrenjun@ihep.ac.cn

development of high-dynamic-range halo monitors and analytical evaluations based upon Campbell's theorem [19, 21]. The later measurements using a diamond-sensor detector indicate that the vertical halo is dominated by the elastic BGS process [22]. Meanwhile, the horizontal halos were much more significant than predicted by BGS and could not be fully explained. Given the relatively large non-zero horizontal dispersion in the arc sections, they were suspected to arise from a scattering process such as Touschek scattering. However, a careful check of this hypothesis could not be pursued due to the lack of an adequate numerical simulation including the necessary physical processes and a powerful monitor for both transverse and longitudinal halos.

In this article, numerical simulations of halo generation, including a complete set of scattering processes in the presence of realistic machine parameters, are presented, followed by direct observations of transverse and longitudinal halos employing a combined yttrium aluminium garnet/optical transition radiation screen monitor. The reasonable agreement between simulation and measurement confirms the Touschek effect's leading role in forming horizontal and momentum halos.

II. ACCELERATOR TEST FACILITY

ATF consists of an electron source based on a Cs_2Te photocathode injector, a 1.3 GeV linac, a damping ring (DR) and an extended extraction line, based on which the ATF2 beam line has been later built. The ATF DR is a race-track type storage ring with a circumference of 138.6 m. It was initially built to demonstrate the production of an ultra-small-emittance beam required at linear colliders. There are 36 FOBO cells in the arc sections, where B represents the combined-function bending magnet. Such a bending magnet can provide a horizontal defocusing field and reduce the horizontal dispersion globally. The phase advances per FOBO cell are $\pi/2$-$5\pi/6$ and $\pi/6$-$\pi/3$, horizontally and vertically, respectively, and can be controlled employing two individual quadrupoles. In the straight sections, several instrumentations have been placed to diagnose beam emittance, beam injection and extraction. Moreover, one RF cavity operating at a frequency of 714 MHz and a cavity-gap voltage of around 300 kV has been integrated to compensate the energy loss due to synchrotron radiation. The smallest vertical emittance of 4 pm has been achieved at a low beam intensity of about 0.16 nC/bunch [13]. Tuning of the low-emittance beam was realized through iterating a series of optics corrections: the closed-orbit-distortion correction, optics matching, dispersion correction and global xy-coupling correction. Thanks to such well-developed tuning techniques, a vertical emittance of around 12 pm can be preserved for daily operation of the ATF DR. The primary parameters of the ATF DR are listed in Table 1.

To demonstrate the feasibility of demagnifying beam to nanometer-scale based on the local-chromaticity-correction scheme and the associated beam handling techniques, the ATF2 project has been launched [14, 23]. ATF2 is an extended extraction line to the ATF damping ring (DR), which supplies a high-quality electron beam with a vertical normalized emittance of about 30 nm, comparable to the requirement of the ILC beam delivery system. The primary goal of ATF2 is to achieve a nanometer beam size with beam orbit stabilization in nanometer precision in the vertical plane at the IP. ATF2 beamline contains three sections: the extraction line (EXT) for the beam extraction and manipulation, the matching section for the adjustment of the downstream optics, and the final focus section (FFS). The EXT section comprises a "dogleg" inflector with two skew-quadrupoles adjacent to the two 10° bends for the vertical dispersion and xy-coupling corrections, an ILC-style coupling correction system consisting of four skew-quadrupoles, and four optical transition radiation (multi-OTR) monitors providing fast diagnostics of emittances and Twiss parameters [24]. Six bipolar quadrupoles in the matching section are for optics matching between the EXT and FFS sections. The FFS compensates the chromaticity locally using two sextupoles adjacent to the final doublet (FD) with non-zero horizontal dispersion generated by upstream bends. Another three sextupoles are placed upstream of the FD in the proper phase with the FD sextupoles to cancel the higher-order aberrations. To loose the tolerance on the magnet multipole errors, a group of skew-sextupoles have been installed in the FFS [25]. Furthermore, two octupoles have been introduced to correct the residual third-order aberrations. Besides, a wakefield compensation setup that contains bellows and a C-band pillbox on mover has been installed in the large β_y region to diminish the downstream beam distortions [26]. For the nanometer beam size diagnostic at the IP, a laser-interferometer beam size monitor has been built at ATF2. Two paths of laser are focused at the IP to form a vertically-oriented interference fringe pattern, the phase of which could be scanned by adjusting the length of one incident laser path. The vertical beam size is then inferred from the modulation depth in the rate of the Compton scattering photons collected by downstream Cherenkov calorimeter-type detector. Thanks to the successful international collaboration, a capability for repeatable tuning of a vertical beam size of less than 60 nm has been successfully demonstrated since 2013 [14, 27].

TABLE 1. ATF main parameters [12, 13].

Beam energy [GeV]	1.3
Circumference [m]	138.6
Bunch charge [nC]	0.16-1.6
Vertical emittance [pm]	>4
Horizontal emittance [nm]	1.2
Energy spread [%]	0.056 (0.08)[a]
Bunch length [mm]	5.3 (7)[a]
Damping time ($x/y/s$) [ms]	17/27/20
Number of bunches	1-20
Repetition rate [Hz]	3.12
RF freqency [MHz]	714

[a] For a bunch charge of 1.6 nC.

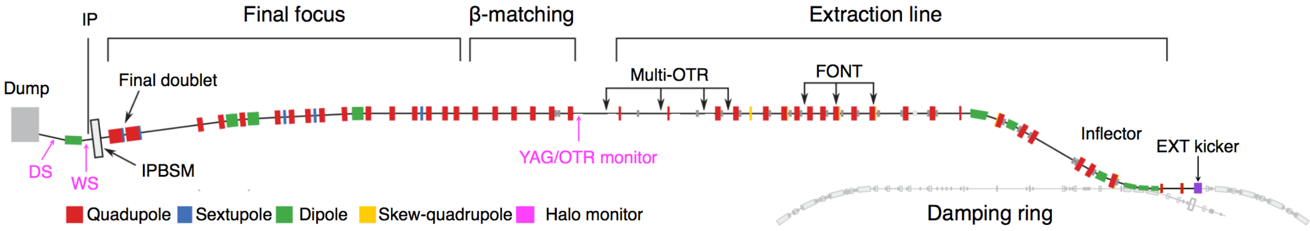

Fig. 1. Schematic layout of the ATF2 beam line.

III. THEORETICAL EVALUATIONS

A. Perturbation by Touschek scattering

Coulomb scattering of particles in bunched beams generates an exchange of momenta between the transverse and longitudinal planes. The multiple small-angle Coulomb scattering, called intra-beam scattering (IBS), diffuses beam-core distribution and leads to dilution of emittance degrading the luminosity of collider or brightness of modern synchrotron radiation light source. The large-angle Coulomb scattering, named Touschek scattering, transfers transverse momentum to the longitudinal and being boosted by a Lorentz factor for the relativistic beam. The resulting momentum perturbation might significantly exceed the longitudinal emittance, thus causing beam halo and particle loss. The Touschek-scattering theories have been investigated as soon as the Touschek effect was for the first time observed in the AdA electron storage ring [28]. Following the A. Piwinski's derivations, the momentum exchange induced by Touschek scattering is re-derived as follows.

The momenta of particles before collision in the laboratory (LAB) coordinate system (s, x, y) are given by

$$\vec{p}_{1,2} = \begin{pmatrix} p_{s1,2} \\ p_{x1,2} \\ p_{y1,2} \end{pmatrix}_{\hat{s},\hat{x},\hat{y}} \tag{1}$$

where $\hat{s}$, $\hat{x}$ and $\hat{y}$ represent the longitudinal, horizontal and vertical unit vector parallel to the s, x and y coordinate axes. We then define a new coordinate system in the LAB frame with the unit vectors $(\hat{u}, \hat{v}, \hat{w})$ which satisfies

$$\hat{u} = \frac{\vec{p}_1 + \vec{p}_2}{|\vec{p}_1 + \vec{p}_2|}, \quad \hat{v} = \frac{\vec{p}_1 \times \vec{p}_2}{|\vec{p}_1 \times \vec{p}_2|}, \quad \hat{w} = \hat{u} \times \hat{v} \tag{2}$$

and the momenta becomes

$$\vec{p}_{1,2} = p_{1,2} \begin{pmatrix} \cos\chi_{1,2} \\ 0 \\ \pm\sin\chi_{1,2} \end{pmatrix}_{\hat{u},\hat{v},\hat{w}} \tag{3}$$

where $\chi_{1,2}$ is the angle between $\vec{p}_{1,2}$ and $\hat{u}$. Applying a Lorentz transformation parallel to $\hat{u}$, we obtain the expression of the momenta in the center-of-mass (COM) coordinate system $(\tilde{u}, \tilde{v}, \tilde{w})$ as

$$\vec{\tilde{p}}_{1,2} = p_{1,2} \begin{pmatrix} \gamma_t(\cos\chi_{1,2} - \frac{\beta_t}{\beta_{1,2}}) \\ 0 \\ \pm\sin\chi_{1,2} \end{pmatrix}_{\hat{\tilde{u}},\hat{\tilde{v}},\hat{\tilde{w}}} \tag{4}$$

where β_t is the relative velocity of the $(\tilde{u}, \tilde{v}, \tilde{w})$ coordinate system and $\beta_{1,2}$ are the relative velocities of the two particles in the laboratory frame

$$\beta_t = \frac{|\vec{p}_1 + \vec{p}_2|c}{E_1 + E_2} = \frac{\beta_1\gamma_1\cos\chi_1 + \beta_2\gamma_2\cos\chi_2}{\gamma_1 + \gamma_2} \tag{5}$$

and the Lorentz factor of the transformation is

$$\gamma_t^2 = \frac{1}{1 - \beta_t^2} \approx \frac{\gamma^2}{1 + \beta^2\gamma^2\chi^2} \tag{6}$$

For the Touschek scattering which induces a large momentum deviation larger than the momentum spread, we further assume that the initial longitudinal projection is small in the $(\tilde{u}, \tilde{v}, \tilde{w})$ coordinate system

$$\xi\sqrt{1 + \gamma^2\chi^2} \ll 2\chi \tag{7}$$

where ξ and χ are defined as

$$\begin{aligned} \xi &= \frac{p_1 - p_2}{\gamma p} \\ \chi^2 &= \frac{(p_{x1} - p_{x2})^2 + (p_{y1} - p_{y2})^2}{4p^2} \end{aligned} \tag{8}$$

where p is the mean momentum, and the momenta in the COM frame are then approximated as

$$\vec{\tilde{p}}_{1,2} \approx \pm\frac{p}{2} \begin{pmatrix} 0 \\ 0 \\ 2\chi \end{pmatrix}_{\hat{\tilde{u}},\hat{\tilde{v}},\hat{\tilde{w}}} \tag{9}$$

The relative velocity of the $(\tilde{u}, \tilde{v}, \tilde{w})$ coordinate system is given by

$$\beta_t = \beta\cos\chi \tag{10}$$

where β is a function of the mean momenta p. The Touschek effect concerns mainly the amount of transverse momentum coupled into the longitudinal direction. Therefore, we define

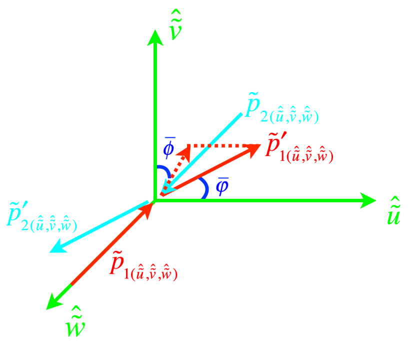

Fig. 2. Schematic of momenta transfer from the transverse plane to the longitudinal direction in the COM frame.

two angles: the polar angle $\bar{\varphi}$ between $\vec{p}^{\prime}_{1,2}$ and $\tilde{u}$-axis, and the azimuthal angle $\bar{\phi}$ between the projection of $\vec{p}^{\prime}_{1,2}$ on the $\tilde{u}\tilde{w}$ plane and the $\tilde{v}$-axis, as shown in Fig. 2. With such definitions, the calculation of the cross section, as well as the magnitude of the momentum transferred into the longitudinal direction, becomes easier. The momenta after a large angle collision in the COM frame are

$$\vec{\tilde{p}}^{\prime}_{1,2} = p\chi \begin{pmatrix} \cos\bar{\varphi} \\ \sin\bar{\varphi}\cos\bar{\phi} \\ \sin\bar{\varphi}\sin\bar{\phi} \end{pmatrix}_{\hat{\tilde{u}},\hat{\tilde{v}},\hat{\tilde{w}}} \tag{11}$$

Then, in the $(u,\ v,\ w)$ coordinate system, the momentum change due to a two-body collision is

$$\vec{p}^{\prime}_{1,2} - \vec{p}_{1,2} = p\chi \begin{pmatrix} \gamma_t\cos\bar{\varphi} \\ \sin\bar{\varphi}\cos\bar{\phi} \\ \sin\bar{\varphi}\sin\bar{\phi} - 1 \end{pmatrix}_{\hat{u},\hat{v},\hat{w}} \tag{12}$$

Finally, the momentum change in the $(s,\ x,\ y)$ coordinate system can be derived as

$$\frac{\delta\vec{p}_{1,2}}{p} = \begin{pmatrix} \chi\gamma_t\cos\bar{\varphi} \\ \frac{\zeta}{2\chi}\sin\bar{\varphi}\cos\bar{\phi} + \frac{\theta}{2\chi}(\sin\bar{\varphi}\sin\bar{\phi} - 1) \\ -\frac{\theta}{2\chi}\sin\bar{\varphi}\cos\bar{\phi} + \frac{\zeta}{2\chi}(\sin\bar{\varphi}\sin\bar{\phi} - 1) \end{pmatrix}_{\hat{s},\hat{x},\hat{y}} \tag{13}$$

where $\bar{\varphi} \in (0, \bar{\varphi}_m)$ and $\bar{\phi} \in (0, 2\pi)$. $\bar{\varphi}_m$ is a function of the momentum acceptance δ_m

$$\bar{\varphi}_m = \cos^{-1}(\delta_m/\gamma_t\chi) \tag{14}$$

Assuming linear synchrotron motion, the perturbations to the kinetic invariant in a dispersive region ($\mathcal{H}_x{\neq}0$, $\mathcal{H}_y{=}0$) are

$$\begin{aligned} \delta J_x =& (\alpha_x x_\beta + \beta_x x^{\prime}_\beta)\frac{\delta p_x}{p} + \frac{\beta_x}{2}\left(\frac{\delta p_x}{p}\right)^2 - \tilde{\eta}_x\frac{\delta p_x}{p}\frac{\delta p}{p} \\ & - [\gamma_x x_\beta\eta_x + \alpha_x\eta^{\prime}_x + x^{\prime}_\beta\tilde{\eta}_x]\frac{\delta p}{p} + \frac{\mathcal{H}_x}{2}\left(\frac{\delta p}{p}\right)^2 \\ \delta J_y =& (\alpha_y y_\beta + \beta_y y^{\prime}_\beta)\frac{\delta p_y}{p} + \frac{\beta_y}{2}\left(\frac{\delta p_y}{p}\right)^2 \\ \delta J_s =& \frac{h\eta_c}{2Q_s}\left[2\frac{\delta p}{p}\frac{\Delta p}{p} + \left(\frac{\delta p}{p}\right)^2\right] \end{aligned} \tag{15}$$

with

$$\begin{aligned} \mathcal{H}_{x,y} &= \eta^2_{x,y} + \tilde{\eta}^2_{x,y} \\ \tilde{\eta}_{x,y} &= \alpha_{x,y}\eta_{x,y} + \beta_{x,y}\eta^{\prime}_{x,y} \end{aligned} \tag{16}$$

where $\beta_{x,y}$, $\alpha_{x,y}$ and $\gamma_{x,y}$ are the Twiss parameters, $\eta_{x,y}$ the dispersion function, $\eta^{\prime}_{x,y} = d\eta_{x,y}/ds$, $\Delta p/p$ the off-momentum coordinate, $\delta p/p$ the momentum change, $\mathcal{H}_{x,y}$ the dispersion invariant, h the harmonic number, η_c the phase-slip factor and Q_s the synchrotron tune. In the presence of the non-zero horizontal dispersion and zero xy coupling, the vertical invariant J_y is only affected via the transverse heating while the horizontal invariant J_x could be enlarged due to the transverse heating and the diffusion coupled through a non-zero $\mathcal{H}_x$. The transverse heating is the analogue of the transverse kicks due to the synchrotron radiation emitted at a small angle to the forward direction. It typically does not result in a large oscillation amplitude.

B. Simulations

The simulation includes three main parts: mimicking realistic beam parameters, generating halo particles from stochastic processes, and particle tracking. The halo generator was developed based on SAD [29]. It initially included only the BGS process [22, 30], and has now been expanded to treat also Touschek scattering.

In contrast to the BGS process, Touschek scattering depends on the local particle density. To reproduce the operational emittances, vertical dispersion and xy coupling are deliberately introduced through local-dispersion bumps and rotations of quadrupoles in the straight sections, respectively, as depicted in Fig. 3. The corresponding sextupole families control chromaticity, while the beta-beat and horizontal-dispersion errors are ignored. For a high-intensity beam, the equilibrium emittance could be significantly diluted due to the intra-beam scattering (IBS) process and are numerically approached through the beam-envelope method [31, 32], as shown in Fig. 4.

Both elastic and inelastic scatterings between particles and nuclei of the residual gas have been included, as described in Ref. [22, 30]. For the sake of simplicity, a uniform gas pressure with CO as the major gas component was assumed. For the Touschek effect, the theory established by Piwinski [33] has been employed to evaluate momentum transformations concerning two-dimensional (2D) particle distributions and variations of beam envelopes in the presence of non-zero dispersion. Piwinski's formulas determine the probability of collisions that result in relative longitudinal momentum changes larger than a minimum acceptance using a Moller scattering cross-section. In the LAB frame, the total cross-section is given by

$$\begin{aligned} \sigma =& \frac{\pi\gamma_t r_e^2}{2\gamma^2}\left[\left(3 - \frac{2}{\tilde{\beta}^2} - \frac{1}{\tilde{\beta}^4}\right)\log\left(\frac{\gamma_t\chi}{\delta_m}\right)\right. \\ & \left. + \left(1 + \frac{1}{\tilde{\beta}^2}\right)^2\frac{\gamma_t^2\chi^2 - \delta_m^2}{\delta_m^2} - \frac{\delta_m}{\gamma_t\chi} + 1\right] \end{aligned} \tag{17}$$

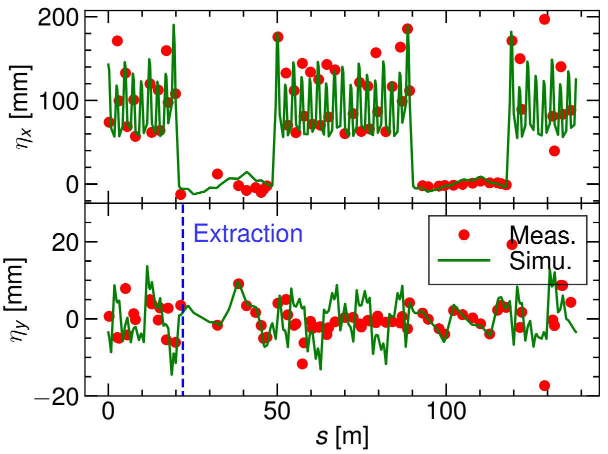

Fig. 3. Reproduction of horizontal and vertical dispersions of the ATF DR via local dispersion bump. The equilibrium vertical emittance is about 12 pm in the presence of intra-beam scattering with a bunch charge of 0.16 nC.

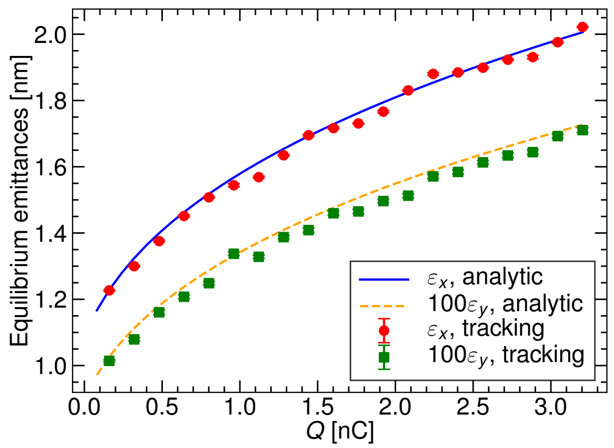

Fig. 4. Equilibrium emittances evaluated by numerical calculation in the presence of synchrotron radiation and IBS, and tracking with one-turn damping and excitation matrices.

where r_e is the classic electron radius, δ_m the minimum momentum perturbation and $\tilde{\beta}$ the relative velocity defined as

$$\tilde{\beta} = \beta\gamma_t\chi \tag{18}$$

For a bunched beam with Gaussian phase-space distributions, the rate of Coulomb scattering leading to a relative longitudinal momentum perturbation of $[\Delta\delta_{\min}, \Delta\delta_{\max}]$ can be expressed as

$$R(\Delta\delta_{\min}, \Delta\delta_{\max}) = R(\Delta\delta_{\min}, \infty) - R(\Delta\delta_{\max}, \infty) \tag{19}$$

with

$$R(\Delta\delta, \infty) = \frac{r_e^2 c N_p^2}{8\pi\gamma^2\sigma_z\sqrt{\sigma_x^2\sigma_y^2 - \eta_x^2\eta_y^2\sigma_\delta^4}\tau_m} F(\tau_m) \tag{20}$$

where c is the velocity of light in vacuum, N_p the bunch population, γ the Lorentz factor, $\sigma_{x,y}$ the transverse beam size, σ_δ the energy spread, σ_z the bunch length and $\tau_m = \beta^2(\Delta\delta)^2$. $F(\tau_m)$ is an integration over the whole beam column, as

$$\begin{aligned} F(\tau_m) =& \sqrt{\pi(B_1^2 - B_2^2)}\tau_m \int_{\tau_m}^{\infty} \Big[\Big(2+\frac{1}{\tau}\Big)^2\Big(\frac{\tau/\tau_m}{1+\tau} - 1\Big) \\ & + 1 - \sqrt{\frac{1+\tau}{\tau/\tau_m}} - \frac{1}{2\tau}\Big(4+\frac{1}{\tau}\Big)\log\Big(\frac{\tau/\tau_m}{1+\tau}\Big)\Big] \\ & e^{-B_1\tau} I_0(B_2\tau)\frac{\sqrt{\tau}d\tau}{\sqrt{1+\tau}} \end{aligned} \tag{21}$$

with

$$\begin{aligned} B_1 &= \frac{\beta_x^2}{2\beta^2\gamma^2\sigma_{x\beta}^2}\Big(1 - \frac{\sigma_h^2\tilde{\eta}_x^2}{\sigma_{x\beta}^2}\Big) + \frac{\beta_y^2}{2\beta^2\gamma^2\sigma_{y\beta}^2}\Big(1 - \frac{\sigma_h^2\tilde{\eta}_y^2}{\sigma_{y\beta}^2}\Big) \\ B_2^2 &= B_1^2 - \frac{\beta_x^2\beta_y^2\sigma_h^2}{\beta^4\gamma^4\sigma_{x\beta}^4\sigma_{y\beta}^4\sigma_\delta^2}(\sigma_x^2\sigma_y^2 - \eta_x^2\eta_y^2\sigma_\delta^4) \\ \frac{1}{\sigma_h^2} &= \frac{1}{\sigma_\delta^2} + \frac{\beta_x\mathcal{H}_x}{\sigma_{x\beta}^2} + \frac{\beta_y\mathcal{H}_y}{\sigma_{y\beta}^2} \\ \tau &= \beta^2\gamma^2\chi^2 \end{aligned} \tag{22}$$

where I_0 is the modified Bessel function, $\sigma_{x\beta,y\beta}$ the betatron beam sizes and $\tilde{\sigma}_{x,y}^2$=$\sigma_{x,y}^2 + \sigma_\delta^2\tilde{\eta}_{x,y}^2$. The resulted momentum perturbations are applied to the core particles, generated randomly based on the equilibrium beam matrices. The local scattering rate is determined considering both the local beam parameters and the distance to the closest upstream element. It should be noted that these calculations assume a significant longitudinal momentum change, and as such, it is important to choose the value of $\Delta\delta$ carefully. The one-dimensional (1D) halo distributions for different minimum momentum changes ($\Delta\delta_{\min}$), from $\sigma_\delta/2$ to $3\sigma_\delta$, have been evaluated and compared, as shown in Fig. 5. The choice of $\Delta\delta_{\min}$ mainly affects the non-Gaussian tails in the 3–6$\sigma_{x,\delta}$ region, where $\sigma_{x,\delta}$ denotes the horizontal beam size or the energy spread. Here, the minimum momentum change has been set as $1\sigma_\delta$ for the following concerns: the horizontal and longitudinal tails in the 3–6$\sigma_{x,\delta}$ region increase by 5.1% and 1.8% as maximum, respectively, when further reducing $\Delta\delta_{\min}$ from $1\sigma_\delta$ to $\sigma_\delta/2$ that, on the other hand, requires two times more computing time. Moreover, the maximum perturbation should be larger than the momentum acceptance ($\sim$1.2%) since some large off-momentum particles might survive for a few turns and slip into the adjacent RF bucket. For simplicity, the transverse heating due to momentum transfers is not included, and therefore, the transverse diffusion takes place only in the dispersive regions.

Scattered particles are tracked element-by-element using the default symplectic tracking routine of SAD. Radiation damping and diffusion from quantum excitation and IBS are applied in a turn-by-turn manner utilizing the corresponding 6×6 excitation matrices. In the ATF damping ring, transverse emittances evaluated analytically are in agreement with the tracking results applying the common excitation matrices, as shown in Fig. 4. The scattered particles are typically gen-

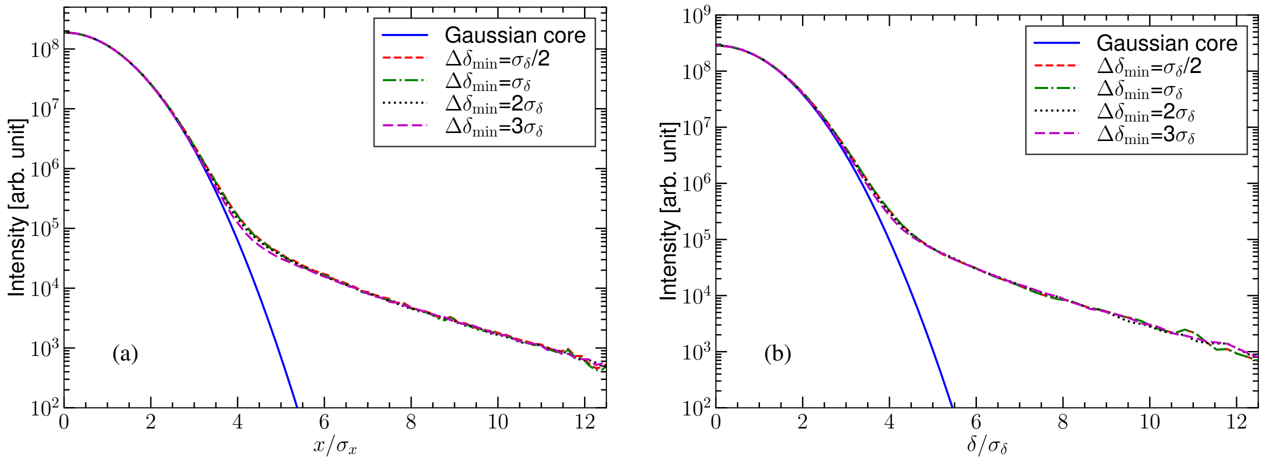

Fig. 5. Evaluations of horizontal (a) and momentum (b) halos versus the bottom limit of the momentum change ($\Delta\delta_{\rm min}$) in the Touschek scattering process.

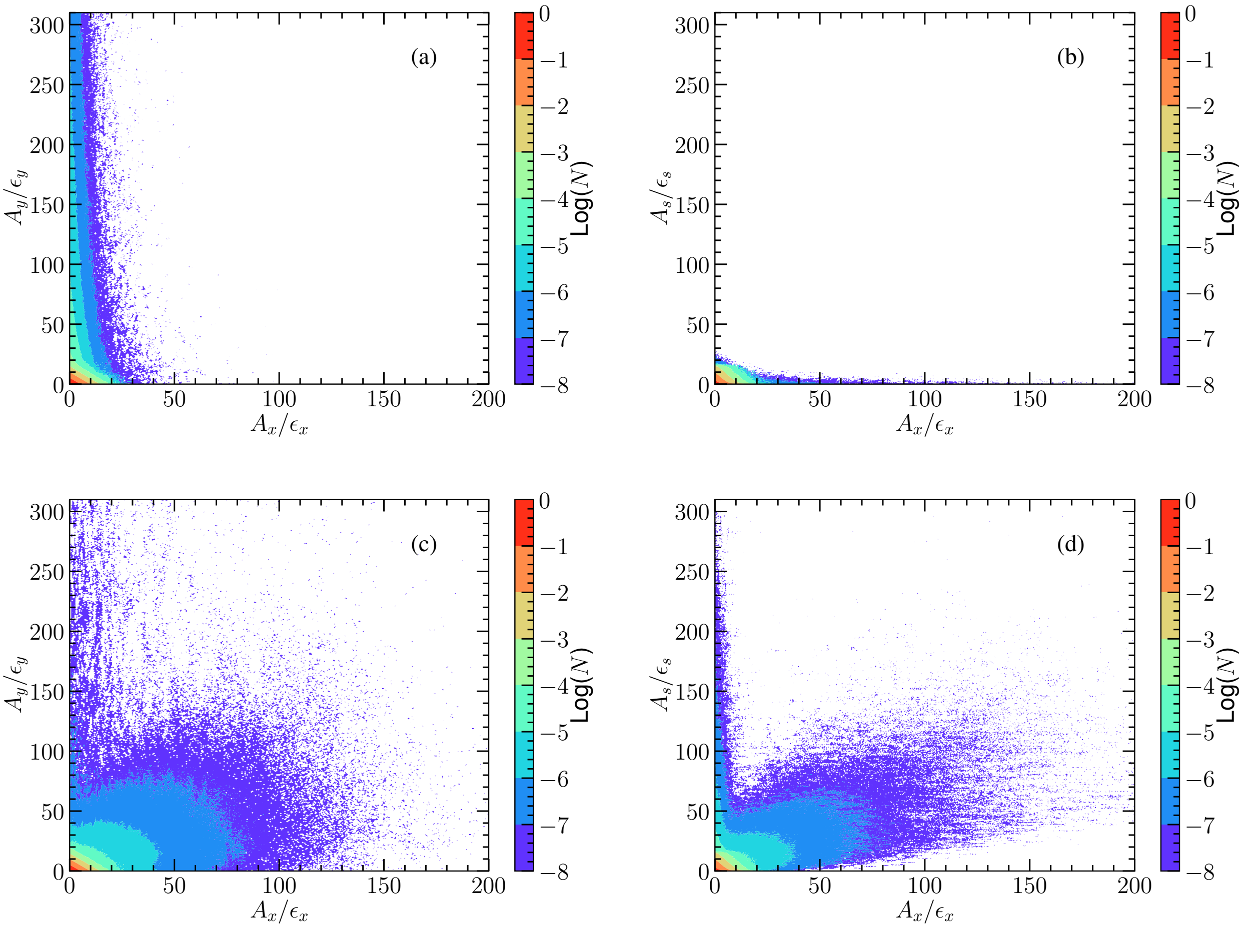

Fig. 6. Two-dimensional beam halos in the presence of different scattering processes: beam-gas scattering (a, b) and Touschek scattering (c, d). The equilibrium vertical, horizontal and longitudinal emittances are 14.0 pm, 1.4 nm and 4.1 μm, respectively, for a bunch charge of 0.48 nC. Moreover, a uniform gas pressure of 2×10^{-7} Pa has been assumed for the BGS process.

erated and tracked for two damping times (about 10^5 turns) to reach equilibrium. Besides, the randomness of quantum and IBS fluctuation allows one to accumulate halo particles over the last few turns for sufficient statistics with a reasonable computing time. The complete distributions are combinations of the scattered particles (more than 1×10^9) and the core particles obtained through tracking in parallel.

The distribution of halo particles in 2D in the presence of both BGS and Touschek scattering processes has been evaluated and is illustrated in Fig. 6. The simulations demonstrate significant horizontal and momentum halos resulting from the Touschek process, while the BGS process mainly governs the formation of the vertical halo. The beam-gas scattering process is primarily elastic, leading to significant vertical halos compared to the horizontal and longitudinal dimensions, as depicted in Fig. 6 (a, b). Touschek scattering events in the dispersive region contribute to the transverse halos, while those in the dispersion-free region form only longitudinal halos. Due to the non-zero horizontal and vertical dispersions in the arcs, transverse halos induced by the Touschek process are correlated, as shown in Fig. 6 (c). In the straight sections, the horizontal dispersion is small, and some longitudinal halos are not coupled into the horizontal plane, as depicted in Fig. 6 (d). Moreover, both 1D and 2D distributions show visible halos up to 10 $\sigma_{x,\delta}$, demanding an instrumentation capable of detecting halos at the level of 10^{-5} of the peak core intensity for the experimental observations.

IV. MEASUREMENTS

A. Experimental setup

There are three types of halo monitors along the ATF2 beamline, i.e., wire scanner (WS), *in-vacuum* diamond sensor (DS) scanner and combined yttrium aluminium garnet (YAG)/optical transition radiation (OTR) monitor. The transverse profiles measured by a carbon wire have been extended with varying voltage of the photomultiplier tube (PMT). Experiments performed at ATF2 have established a dynamic range of about 10^4, limited by the remaining background due to beam loss along the ATF2 beamline. The DS scanner has four chemical-vapor-deposition (CVD) single-crystal strips on a ceramic printed circuit board (PCB). Aiming to obtain a higher dynamic range, two narrow strips of 0.1×4 mm^2 and two broad ones of 1.5×4 mm^2 for the core and halo measurements, respectively, have been designed. Typically, the strips are biased to -400 V for collecting the electron-hole pairs generated from the ionization process. Due to the space-charge effect inside the diamond crystal bulk and the instantaneous voltage drop at the resister, the readout signal can be significantly distorted when the diamond strip travels into the core region. To overcome such issues, a rescaling scheme based upon additional calibration using an adjacent wire scanner has been implemented to reconstruct the core profile. And, an effective dynamic range of 10^5 has been eventually obtained [22]. However, halo diagnostics using wire or DS scanners are time-consuming (about 30 minutes for 1D imagination) to meet the required resolution and accuracy.

For fast halo diagnostics, a combined YAG/OTR monitor has been developed and installed in the extraction line of ATF [34]. The favourable scintillating properties of cerium-doped YAG, for instance, the high photon yield (about 2×10^4 ph/MeV), fast emission decay (decay time constants of 88 and 300 ns), mechanical rigidity and radiation hardness, have made it being one popular scintillator for two-dimensional imaging of energetic charged particles and photons, especially low-density particles distributions. On the other hand, the scintillation saturation of Ce:YAG from more densely populated incident beams has to be avoided or compensated by supplementary diagnostics. Following these considerations, four 0.5 mol% Ce:YAG screens with a central rectangular opening for visualising core and halo profiles and an OTR target providing supplementary visualisation of the dense beam core have been constructed. Scintillation light and transition radiation can be alternately collected through a fused silica viewport and focused on the camera sensor, as depicted in Fig. 7. The YAG pads and rectangular opening sizes are $4\times6\times0.1$ mm^3 and 4×2.4 mm^2, respectively. The OTR target consists of an aluminium kapton of 2 μm thickness seated in a titanium conical receptacle, leaving an exposed area of 7 mm diameter. The screens are placed on a holder actuated by an automatic manipulator. For halo imaging, one must adjust the YAG pads to allow core particles to pass through the central opening. The YAG and OTR screens are at 45° and 67.5° to the beam trajectory, respectively, to collect scintillating and backward OTR light with a common optical system comprising neutral-density filters, a microscope lens and a 16-bit cooled complementary metal-oxide-semiconductor (sCMOS) camera. The optical system is -45° to beam direction and perpendicular to the YAG screen. In the sequence, the depth-of-field limitation of the microscope is loosened to 0.13 mm. Considering the size of the camera sensor (13.3×13.3 mm^2) and the required field of view ($10\sigma_{x,y}$), the magnification factor of the microscope lens was set at 2.5-3, which is determined by correlating the observed holder edge movement versus the manipulator position readout. The backlash and readout accuracy of the four-dimensional manipulator ($\vec{x}$, $\vec{y}$, $\vec{s}$ and rotation around $\vec{s}$-axis) were found to be about 13.5 μm and less than 0.2 μm, respectively, which allow precise determination of magnification factor. Besides, an interface has been developed in Python for data acquisition and remote control.

The lower limit of the dynamic range is primarily determined by three factors: the Photon Yield (PhY) of the Ce:YAG, the photon collection efficiency and the background noise. The YAG scintillation saturation sets an upper limit to the dynamic range, which the OTR screen can further improve. Monte Carlo simulations in MCNPX predict that energy deposition inside the YAG pad is about 0.1–0.12 MeV/e for a beam energy of 1.3 GeV. Assuming a PhY of 2×10^4 ph/MeV, the photon emission is estimated at 2000–2500 ph/e, and the photon collection is evaluated as 0.32–4 ph/e. This estimation considers a light transmission of around 85% in the optical observation system and an effec-

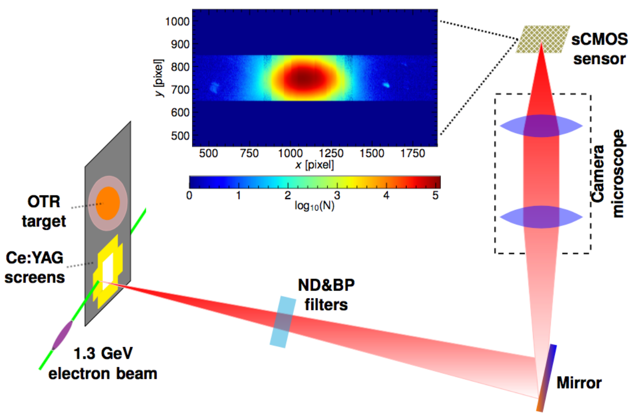

Fig. 7. Schematic of the YAG/OTR monitor including a 2D core-halo image obtained through horizontal scanning of the left and right YAG pads. The glare in the halo region are from dust on the screen.

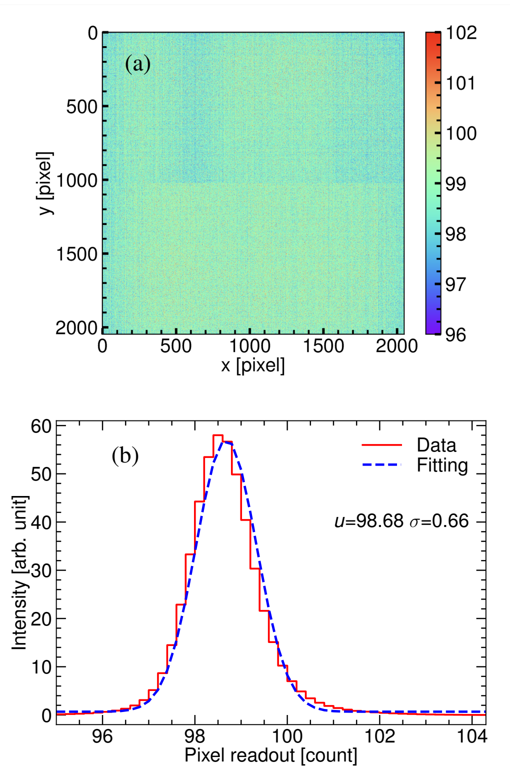

Fig. 8. A background image (a) and the histogram of dark count (b) in the rolling shutter mode with an exposure time of 10 ms.

tive observation angle of 6.2 mrad. Notice that the refraction of light exiting the YAG screen induces a smaller observation angle, which can be evaluated as [35]

$$\theta' = \arcsin(n_1/n_2 \sin\theta) \tag{23}$$

where n_1 and n_2 are the refractive indices of vacuum and YAG, respectively, and θ is the acceptable angle of the observation system. The sCMOS camera was placed at 300 mm above the beam line to reduce the beam-induced background. However, noise from the camera sensor is unavoidable, dependent on its temperature (10 °C with the cooling system), the exposure mode and the exposure time. Typically, the camera was operated in the rolling shutter mode with an exposure time of 10 ms. A non-uniform noise level for each pixel has been observed with a noise level of less than one digital count, as shown in Fig 8. Subtracting a constant noise level, the residual background level was found to be less than 0.5 count/pixel, i.e., 0.33 ph/pixel in terms of the nominal quantum efficiency of 70% and the A/D conversion of 0.46 e/count. To obtain a signal-noise-ratio (SNR) larger than three, at least one incident photon on a single pixel, i.e., a minimum particle density of 4 electrons over one pixel-equivalent size on the YAG screen, is required. The maximum particle density in the absence of scintillation saturation is characterized by the saturation threshold, which is challenging to quantify analytically. Therefore, experimental measurements of the saturation threshold have been conducted at KEK-ATF. During quadrupole scanning, beam sizes and fluxes of scintillation light were measured to determine the saturation threshold by the maximum local particle density (at the beam center) at the transition between saturation and no saturation. Here, the beam core is always assumed to be distributed according to a Gaussian function. For a beam intensity of 3×10^9 e/pulse, the flux of collected scintillating light tends to remain constant (around $1.2{\times}10^9$ photons) when the vertical beam size is large. Then, it decreases due to scintillation saturation when focusing the vertical beam size down to 40 μm, as shown in Fig. 9. The saturation threshold is therefore found to be 16–18 fC/μm^2. Correspondingly, for a magnification factor of 2.5, the effective particle density is expected to be about $4.8{\times}10^5$ e/pixel without saturation, which implies a dynamic range of approximately $1{\times}10^5$ imaging with YAG screens.

To avoid blooming effects, halo distributions are measured through one-dimensional scans of the YAG pads. After taking a picture of the halo far from the beam core, the YAG pads are moved toward the beam core step-by-step and images are captured with light attenuation at each step. Then, sliced halo images at different distances to the center are cut out by trimming the parts near the inner edge of the YAG, overlapping with preceding images. Eventually, a complete core-halo distribution is obtained by combining the core and the sliced halo images of the two sides, as illustrated in Fig. 7. Owing to this scanning procedure, vertical and horizontal profiles have to be captured individually. Using solely the YAG screens, a dynamic range of about $1{\times}10^5$, limited by the photon-yield efficiency of the scintillator, background noise and scintillation saturation, has been demonstrated.

For the observation of the momentum halo, the optical dispersion at the diagnostic point must be modulated to dominate the transverse beam profile. To characterise the resolution of the momentum visualisation, the least distinguishable energy spread can be defined by

$$\delta_{\min} = 2\sqrt{\varepsilon_{x,y}\beta_{x,y}}/\eta_{x,y} \tag{24}$$

where $\varepsilon_{x,y}$ is the transverse emittance. Apparently, a small

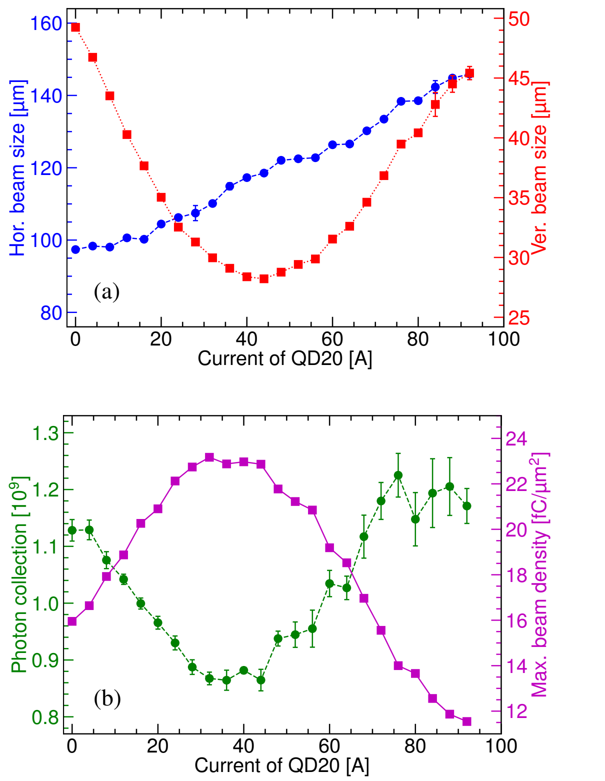

Fig. 9. Evolution of vertical and horizontal beam sizes (a), number of collected photons and maximum beam density (b) as a function of the upstream quadrupole (QD20) current. Notice that the saturation threshold is given by the maximum particle density at 75 A.

$\sqrt{\beta}/\eta$ ratio, which can be realised through careful tuning of linear beam optics, will be necessary to improve the momentum resolution. For the ATF2 beam, the vertical emittance is typically only 1% of the horizontal emittance, and the visualisations in the "vertical" plane will be favoured. As a result, the YAG/OTR monitor has been placed downstream of a dogleg inflector in the extraction line. A large vertical dispersion (>200 mm) can be easily bumped using two skew-quadrupoles located in the dogleg where the horizontal dispersion reaches its largest absolute values but with opposite signs, as shown in Fig. 10. Thanks to the appropriate phase advances between the two skew-quadrupoles (2π and π for the horizontal and vertical planes, respectively), a small β-function (about 4 meters) at the observation point can be well preserved while manipulating the downstream vertical dispersion. Regarding the typical ATF2 beam parameters, tracking simulations have suggested a vertical dispersion of larger than 160 mm for picturing the momentum spectrum. In reality, through the comparisons of the "vertical" profiles predicted by tracking simulation and observed by the YAG/OTR monitor, as well as the observations of vacuum dependency with different vertical dispersions, we have concluded that a vertical dispersion of above 200 mm would offer the expected representation of the momentum spectrum.

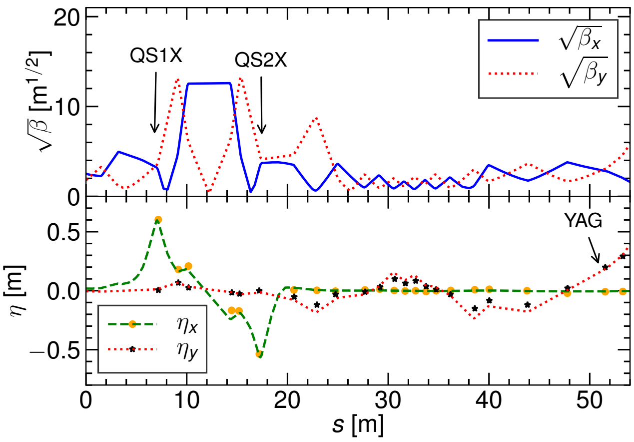

Fig. 10. Beta-function and dispersion along the extraction line. The colored marks represent the experimental data and the lines denote the model optics. QS1X and QS2X are the skew-quadrupoles for vertical-dispersion control.

B. Transverse and longitudinal halos

The vertical halo was already shown in a previous study to be primarily driven by the elastic BGS process [22]. Therefore, only the horizontal and momentum halo measurements are presented here.

As shown in Fig. 11 (a-b), the measured horizontal halos are in reasonable agreement with the simulations for varying gas pressures (2×10^{-7}-1.2×10^{-6} Pa) and bunch charges (0.16-0.96 nC). Although the DR vacuum level has a negligible impact on horizontal halos, a higher bunch charge significantly enhances them. The measurements only extend to 8-10σ due to background noise near the edges of the camera sensor. It is apparent that measurements away from the beam core are already noisy, especially for low bunch charges. The relative residuals of horizontal halos have also been evaluated, and the averages of relative residuals for horizontal halos in the 4-8σ_x region is below 0.34±0.12, as indicated in Table 2.

TABLE 2. Relative residual of the observed horizontal halos over the 4-8σ_x region.

Pressure [Pa]	Bunch charge [nC]	Relative residual
	0.16	0.11±0.45
2×10^{-7}	0.48	0.08±0.10/0.34±0.12[a]
	0.96	-0.10±0.07
1.2×10^{-6}	0.48	0.04±0.08

[a] Data obtained with different beam emittances.

The momentum halos are imaged in the vertical plane with a vertical dispersion of about 200 mm at the YAG/OTR monitor. The potential impact of the vertical betatron halo requires a thorough evaluation. The observations at two different gas pressures (2×10^{-7} and 1.2×10^{-6} Pa) show good agreement with numerical simulations and insignificant correlation with

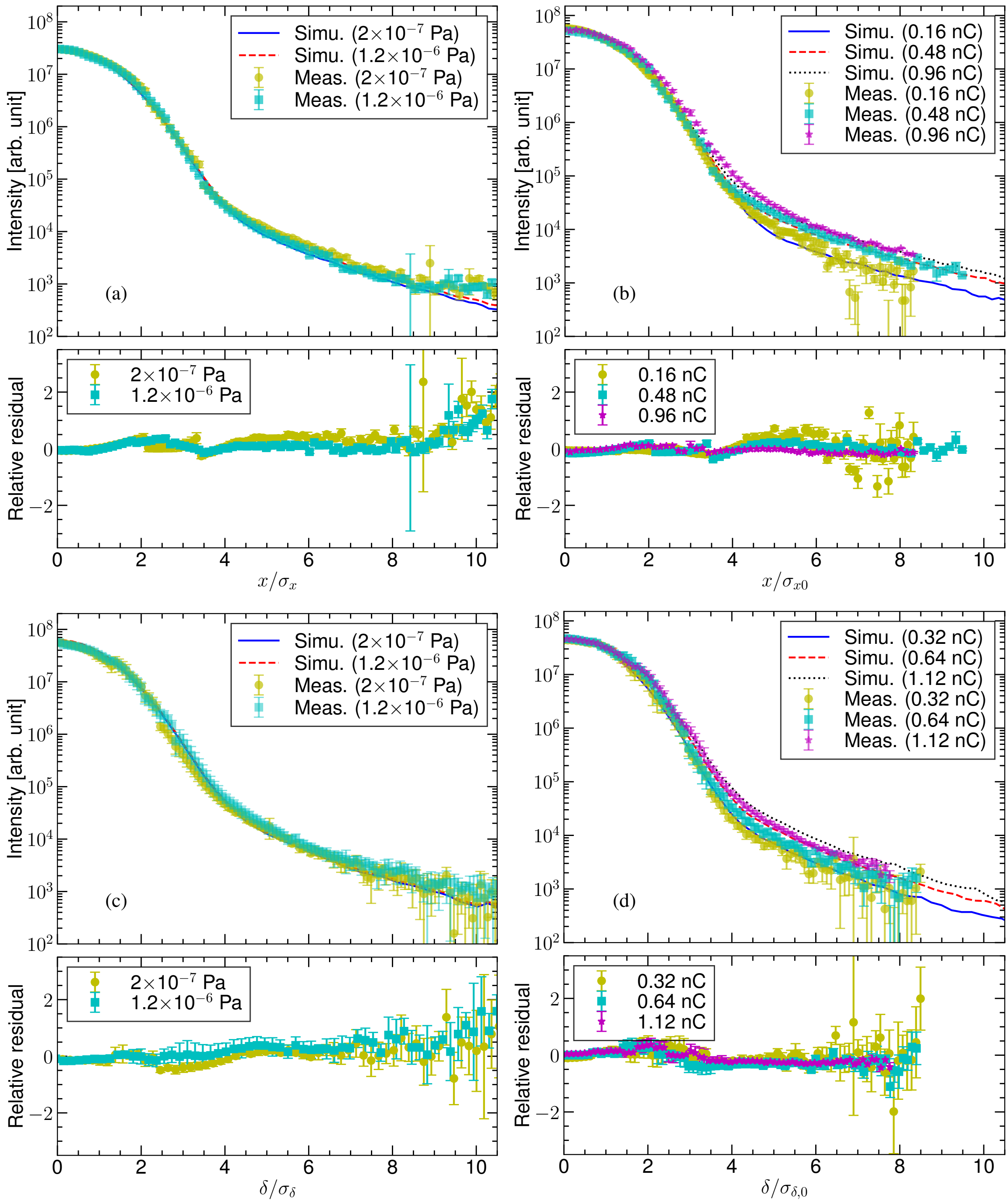

Fig. 11. Normalized horizontal (a, b) and momentum (c, d) halos for different gas pressures and bunch charges. Notice that a bunch charge of 0.48 nC is used for the vacuum-dependence studies. $\sigma_{x,0}$ represents horizontal beam size for a bunch charge of 0.48 nC and $\sigma_{\delta,0}$ is the energy spread at a bunch charge of 0.32 nC.

the gas pressure, as shown in Fig. 11 (c). The averages of relative residuals over the 4-8σ_δ region are 0.02±0.20 and 0.31±0.21 for the two gas pressures, respectively, as shown in Table 3. These presences indicate a negligible contribution from the vertical betatron halo that has been verified to be proportional to the DR gas pressure. Although the observations suggest a weaker intensity dependence than the numerical predictions, but the observed trends are consistent, as shown in Fig. 11 (d). The averages of relative residuals over the 4-8σ_δ region are -0.11±0.44, -0.30±0.17 and -

TABLE 3. Relative residual of the observed momentum halos over the 4-8σ_δ region.

Pressure [Pa]	Bunch charge [nC]	Relative residual
2×10^{-7}	0.32	-0.11±0.44
	0.48	0.02±0.20
	0.64	-0.30±0.17
	1.12	-0.24±0.06
1.2×10^{-6}	0.48	0.31±0.21

0.25±0.06 for bunch charges of 0.32, 0.64 and 1.12 nC, respectively, as shown in Table 3. Due to a limited sensitivity of the YAG/OTR monitor, the obtained momentum halos at low bunch charges (<0.32 nC) exhibit visible fluctuations.

The congruence between measurements and simulations, along with the anticipated dependencies on gas pressure and bunch charge, strongly indicate Touschek scattering as the predominant factor contributing to the formation of horizontal and momentum halos. The residual discrepancies between predictions and observations might be attributed to the systematic uncertainty related to the instrumentation and the modelling of particle beam. The instrumentation-related uncertainty can plainly be seen in the observed halos far from the beam center, especially at a low bunch charge. In addition, the numerical predictions could be influenced by other factors, such as uncertainties in vertical emittance measurements, errors in mimicking the realistic machine parameters, and ambiguities in the calculations of beam emittances and diffusion maps. Even a slight error in the model vertical emittance can cause notable differences in equilibrium beam sizes, Touschek scattering rate, and ultimately, predicted horizontal and momentum halo distributions, as shown in Fig. 12.

An underestimated model vertical emittance for the numerical predictions may thus partly explain the discrepancy between the observations and simulations at high bunch charges. More comprehensive measurements of emittances, bunch length and energy spread are needed as input to the simulations to improve the comparisons with the measurements. Moreover, halo distributions may be affected by nonlinearities in the damping ring and multipoles of the extraction kicker, which should also be considered for future investigations.

V. CONCLUSION

The origin of the horizontal and momentum halos has been theoretically and experimentally studied for the KEK-ATF. To this end, a halo generator containing diffusions, BGS and Touschek scattering processes has been developed in a simulation approach based on realistic operational beam parameters. Moreover, a combined YAG/OTR monitor has been designed and installed to measure the vertical, horizontal, and momentum halos. The reasonable consistencies between observations and simulations for various gas pressures and bunch charges indicate that the Touschek scattering dominates horizontal and momentum halos. Some observed resid-

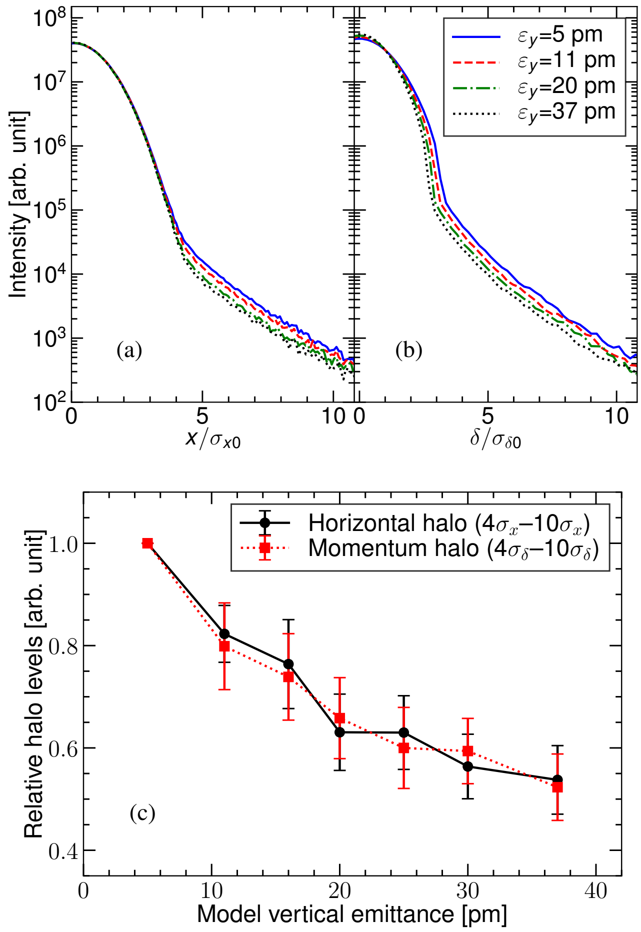

Fig. 12. Horizontal and momentum halos (a, b), and relative halo levels (c) for different vertical emittances with a bunch charge of 0.96 nC. σ_{x0} and $\sigma_{\delta 0}$ are horizontal beam size and momentum spread, respectively, for a vertical emittance of 11 pm.

ual discrepancies might be attributed to the residual imperfection in modelling beam emittances. Further simultaneous measurements of emittances and beam halos employing an improved monitor with a higher dynamic range ($\gtrsim 10^6$) at the controlled vertical emittance would be recommended.

These observations provide a reliable benchmark of the halo generator and validate its applicability to modern GeV-scale low-emittance storage rings. Future improvement of this numerical tool concentrates on the modelling of particle beam and accelerators with better accuracy and completeness.

VI. ACKNOWLEDGEMENTS

The authors would like to express their gratitude to the ATF2 collaboration and the staff of ATF. We also thank K. Oide, T. Lefèvre, S. Mazzoni, R. Nagaoka and D. Zhou for many helpful discussions and continuous encouragement.

[1] A. Aleksandrov, S. Cousineau, K. Ruisard *et al*, First measurement of a 2.5 MeV RFQ output emittance with 1 part-per-million dynamic range, Nucl. Instrum. Methods Phys. Res., Sect. A **987**, 164829 (2021). doi: 10.1016/j.nima.2020.164829

[2] K. Hirata, K. Yokoya, Non gaussian distribution of electron beams due to incoherent stochastic processes, Part. Accel. **39**, 147–158 (1992).

[3] T. Chen, J. Irwin, R. Siemann, Simulation of the beam halo from the beam-beam interaction, Phys. Rev. E **49**, 2323-2330 (1994). doi: 10.1103/PhysRevE.49.2323

[4] H. Burkhardt, I. Reichel, G. Roy, Transverse beam tails due to inelastic scattering, Phys. Rev. ST Accel. Beams **3**, 091001 (2000). doi: 10.1103/PhysRevSTAB.3.091001

[5] H. Burkhardt, I. Ahmed, M. Fitterer *et al*, Halo and tail generation computer model and studies for linear colliders, EUROTeV-Report-2008-076 (2008).

[6] R. Gluckstern, Analytic Model for Halo Formation in High Current Ion Linacs, Phys. Rev. Lett. **73**, 1247 (1994). doi: 10.1103/PhysRevLett.73.1247

[7] C. Allen, K. Chan, P. Colestock *et al*, Beam-halo measurements in high-current proton beams, Phys. Rev. Lett. **89**, 214802 (2002). doi: 10.1103/PhysRevLett.89.214802

[8] K. Oide, H. Koiso, Anomalous equilibrium emittance due to chromaticity in electron storage rings, Phys. Rev. E **49**, 4474 (1994). doi: 10.1103/PhysRevE.49.4474

[9] M. Ikegami, S. Machida, T. Uesugi, Particle-core analysis of dispersion effects on beam halo formation, Phys. Rev. ST Accel. Beams **2**, 124201 (1999). doi: 10.1103/PhysRevLett.115.204802

[10] I. Hofmann, O. Boine-Frankenheim, Space-Charge Structural Instabilities and Resonances in High-Intensity Beams, Phys. Rev. Lett. **115**, 204802 (2015). doi: 10.1103/PhysRevLett.115.204802

[11] K. Wittenburg, Beam halo and bunch purity monitoring, arXiv:2005.07027 (2020). doi: arXiv:2005.07027

[12] K. Kubo, M. Akemoto, S. Anderson *et al*, Extremely Low Vertical-Emittance Beam in the Accelerator Test Facility at KEK, Phys. Rev. Lett. **88**, 194801 (2002). doi: 10.1103/PhysRevLett.88.194801

[13] K. Honda, K. Kubo, S. Anderson *et al*, Achievement of Ultralow Emittance Beam in the Accelerator Test Facility Damping Ring, Phys. Rev. Lett. **92**, 054802 (2004). doi: 10.1103/PhysRevLett.92.054802

[14] G. White, R. Ainsworth, T. Akagi *et al*, Experimental validation of a novel compact focusing scheme for future energy-frontier linear lepton colliders, Phys. Rev. Lett. **112**, 034802 (2014). doi: 10.1103/PhysRevLett.112.034802

[15] A. Aryshev, P. Bambade, D. Bett *et al*, ATF Report 2020, CERN-ACC-2020-0029 (2020).

[16] M. Boscolo, P. Raimondi, Monte Carlo simulation for the Touschek effect with the crab-waist scheme, Phys. Rev. ST Accel. Beams **15**, 104201 (2012). doi: 10.1103/PhysRevSTAB.15.104201

[17] J. Breunlin, S. Leemann, A. Andersson, Improving Touschek lifetime in ultralow-emittance lattices through systematic application of successive closed vertical dispersion bumps, Phys. Rev. Accel. Beams **19**, 060701 (2016). doi: 10.1103/PhysRevAccelBeams.19.060701

[18] A. Natochii, S. Vahsen, H. Nakayama *et al*, Improved simulation of beam backgrounds and collimation at SuperKEKB, Phys. Rev. Accel. Beams **24**, 081001 (2021). doi: 10.1103/PhysRevAccelBeams.24.081001

[19] S. Liu, F. Bogard, P. Cornebise *et al*, In vacuum diamond sensor scanner for beam halo measurements in the beam line at the KEK Accelerator Test Facility, Nucl. Instrum. Methods Phys. Res., Sect. A **832**, 231 (2016). doi: 10.1016/j.nima.2016.06.122

[20] T. Naito, H. Hayano, K. Kuroda *et al*, Emittance measurements using a X-ray beam profile monitor at KEK-ATF, in *IBIC2012*, Tsukuba, Japan 2017. pp. 215–217

[21] D. Wang, J. Gao, P. Bambade *et al*, Analytical estimation of ATF beam halo distribution, Chin. Phys. C **38**, 127003 (2014). doi: 10.1088/1674-1137/38/12/127003

[22] R. Yang, T. Naito, S. Bai *et al*, Evaluation of beam halo from beam-gas scattering at the KEK Accelerator Test Facility, Phys. Rev. Accel. Beams **21**, 051001 (2018). doi: 10.1103/PhysRevAccelBeams.21.051001

[23] P. Raimond, A. Seryi, Novel Final Focus Design for Future Linear Colliders, Phys. Rev. Lett. **86**, 3779 (2001). doi: 10.1103/PhysRevLett.86.3779

[24] A. Faus-Golfe, J. Navarro, N. Fuster Martinez *et al*, Emittance reconstruction from measured beam sizes in ATF2 and perspectives for ILC, Nucl. Instrum. Methods Phys. Res., Sect. A **819**, 122 (2016). doi: 10.1016/j.nima.2016.02.064

[25] T. Okugi, S. Araki, P. Bambade *et al*, Linear and second order optics corrections for the KEK Accelerator Test Facility final focus beam line, Phys. Rev. ST Accel. Beams **17**, 023501 (2014). doi: 10.1103/PhysRevSTAB.17.023501

[26] J. Snuverink, R. Ainsworth, S. Boogert *et al*, Measurements and simulations of wakefields at the Accelerator Test Facility 2, Phys. Rev. Accel. Beams **19**, 091002 (2016). doi: 10.1103/PhysRevAccelBeams.19.091002

[27] R. Yang, A. Pastushenko, A. Aryshev *et al*, Tuning the ultralow β^* optics at the KEK Accelerator Test Facility 2, Phys. Rev. Accel. Beams **23**, 071003 (2020). doi: 10.1103/PhysRevAccelBeams.23.071003

[28] C. Bernardini, G. Corazza, G. Di Giugno *et al*, Lifetime and Beam Size in a Storage Ring, Phys. Rev. Lett. **10**, 407 (1963). doi: 10.1103/PhysRevLett.10.407

[29] SAD, is a computer program for accelerator design, see http://acc-physics.kek.jp/SAD/

[30] R. Yang, P. Bambade, K. Kubo *et al*, Numerical investigation of beam halo from beam gas scattering in KEK-ATF, Journal of Physics: Conference Series **874**, 012063 (2017). doi: 10.1088/1742-6596/874/1/012063

[31] K. Ohmi, K. Hirata, K. Oide, From the beam-envelope matrix to synchrotron-radiation integrals, Phys. Rev. E **49**, 752 (1994). doi: 10.1103/PhysRevE.49.751

[32] K. Kubo, K. Oide, Intrabeam scattering in electron storage rings, Phys. Rev. ST Accel. Beams **4**, 124401 (2001). 10.1103/PhysRevSTAB.4.124401

[33] A. Piwinski, The Touschek effect in strong focusing storage rings, arXiv:physics/9903034 (1999). doi: 10.48550/arXiv.physics/9903034

[34] R. Yang, T. Naito, S. Wallon *et al*, Development of a YAG/OTR Monitor, in *IBIC2018*, Shanghai, China, 2018. pp. 499–502

[35] A. Murokh, J. Rosenzweig, V. Yakimenko *et al*, Limitations on the resolution of YAG: Ce beam profile monitor for high brightness electron beam, in *The Physics of High Brightness Beams*, ed. by J. Rosenzweig, L. Serafini (World Scientific, Los Angeles, 2000), pp. 564–580